

Mass-loss rates from mid-infrared excesses in LMC and SMC O stars

D. Massa,^{1★} A. W. Fullerton^{2★} and R. K. Prinja^{3★}

¹Space Science Institute, Boulder, CO 80301, USA

²Space Telescope Science Institute, Baltimore, MD 21218, USA

³Department of Physics and Astronomy, University College London, Gower Street, London WC1E 6BT, UK

Accepted 2017 June 7. Received 2017 June 4; in original form 2017 April 18

ABSTRACT

We use a combination of *BVJHK* and *Spitzer* [3.6], [5.8] and [8.0] photometry to determine infrared (IR) excesses for a sample of 58 Large Magellanic Cloud and 46 Small Magellanic Cloud O stars. This sample is ideal for determining IR excesses because the very small line-of-sight reddening minimizes uncertainties due to extinction corrections. We use the core–halo model developed by Lamers & Waters to translate the excesses into mass-loss rates and demonstrate that the results of this simple model agree with the more sophisticated CMFGEN models to within a factor of 2. Taken at face value, the derived mass-loss rates are larger than those predicted by Vink et al., and the magnitude of the disagreement increases with decreasing luminosity. However, the IR excesses need not imply large mass-loss rates. Instead, we argue that they probably indicate that the outer atmospheres of O stars contain complex structures and that their winds are launched with much smaller velocity gradients than normally assumed. If this is the case, it could affect the theoretical and observational interpretations of the ‘weak wind’ problem, where classical mass-loss indicators suggest that the mass-loss rates of lower luminosity O stars are far less than expected.

Key words: stars: early-type – stars: winds, outflows – Magellanic Clouds.

1 INTRODUCTION

The winds of massive stars power and enrich the ISM, affect the evolution of the stars, determine their ultimate fate and the nature of their remnants, influence the appearance of the integrated spectra of young, massive clusters and starbursts and play a major role in the initial stages of massive star cluster formation and their subsequent evolution. Consequently, reliable measurements of mass-loss rates due to stellar winds are essential for all of these subjects.

Stellar winds are driven by radiative pressure on metal lines (Castor, Abbott & Klein 1975, hereafter **CAK**). However, in recent years, it has become apparent that the winds are far more complex than the homogeneous, spherically symmetric flows envisioned by **CAK**. Instead, they have been shown to contain optically thick structures that may be quite small or very large. Further, these structures are thought to have non-monotonic radial velocities. Corotating interaction regions (Cranmer & Owocki 1996; Lobel & Blomme 2008) are examples of large structures and wind fragments caused by the line deshadowing instability (Owocki, Castor & Rybicki 1988; Sundqvist, Puls & Feldmeier 2010; Šurlan et al. 2012) are examples of small structures. Until the details of these flows are unraveled, we cannot reliably translate observational diagnostics into physical quantities such as mass-loss rates. To progress, a firm grasp

on the underlying physical mechanisms that determine the wind structures is required. The state of affairs can be seen in recent literature where the values of observationally derived mass-loss rates have swung back and forth by factors of 10 or more (Massa et al. 2003; Fullerton, Massa & Prinja 2006; Puls et al. 2006; Sundqvist et al. 2010; Šurlan et al. 2012).

Evidence for large-scale wind structure first emerged when the variability was observed in H α line profiles (Underhill 1961; Rosendhal 1973a,b; Ebbets 1982). This was followed by studies of ultraviolet (UV) P Cygni line variability by several investigators, who examined the behaviour of discrete absorption components, which traverse UV wind line profiles and suggest the presence of large, coherent structures propagating through the winds (e.g. Kaper et al. 1999; Prinja, Massa & Fullerton 2002). Similar features are observed in Large Magellanic Cloud (LMC) and Small Magellanic Cloud (SMC) O stars (Massa et al. 2000) and in planetary nebula central stars (Prinja et al. 2012), suggesting these structures are a universal property of radiatively driven flows.

Perhaps the most compelling evidence that the winds contain optically thick structures was provided by Prinja & Massa (2010), who used doublet ratios to demonstrate that apparently unsaturated wind lines often arise in structures that are optically very thick, but cover only a fraction of the stellar surface. Further, Massa & Prinja (2015) used UV excited state wind lines to demonstrate that at least some of these structures are quite large and originate very near or on the stellar surface. Additional evidence for large-scale

* E-mail: dmassa@space.science.org (DM); fullerton@stsci.edu (AWF); rkp@star.ucl.ac.uk (RKP)

structure has been deduced from X-ray variability (e.g. Massa et al. 2014; Rauw et al. 2015). Models that account for optically thick structures have been developed (Sundqvist et al. 2010; Šurlan et al. 2012), and they provide somewhat better descriptions of the observations. However, one must keep in mind that whenever optically thick structures are included in a model, *geometry matters*. Therefore, it is essential to constrain the shape of the structures as much as possible, and the best way to probe the geometry is to examine all of the spectral diagnostics available. Only when all of the available diagnostics have been examined, and a model constructed that can simultaneously explain them all, will we be assured that observationally determined mass-loss rates are meaningful. Each diagnostic provides an important piece of the puzzle.

The IR fluxes of OB stars present an important diagnostic that has been largely neglected. It was shown early on that emission from OB star winds should be detectable at infrared (IR) and radio wavelengths (Panagia & Felli 1975; Wright & Barlow 1975). This realization spawned observations of OB stars at near and mid-IR wavelengths (e.g. Castor & Simon 1983; Abbott, Telesco & Wolff 1984), but the results were considered untrustworthy for two reasons. First, IR photometric systems were still evolving at the time and poorly calibrated. As a result, only rather large excesses could be trusted. Secondly, accurate reddening corrections are essential for interpreting IR excesses, since the excess must be measured relative to the stellar flux at a wavelength assumed to be free of wind emission, typically *V*-band photometry. However, there are very few lightly reddened, luminous Galactic OB stars, and the exact form of the IR reddening law was poorly characterized at the time of the early studies. Nevertheless, there remains strong motivation to study IR excesses since, as Puls et al. (2006) demonstrated, the wavelength dependence of the mid-IR spectral energy distribution (SED) can provide important information on the radial dependence of clumping in the wind.

This paper has two major goals. The first is to use near-IR (NIR) and mid-IR observations of Magellanic cloud O stars to determine their IR excesses and compare them to theoretical expectations. The second is to compare the IR mass-loss rates of LMC and SMC stars to examine how metallicity affects the results. In Section 2, we describe our sample of stars. In Section 3, we derive the physical parameters of the stars and quantify the influence of interstellar extinction. In Section 4.1, we motivate, describe and justify the simplified model we use to derive mass-loss rates from IR excesses. In Section 5, we describe how we fit the IR photometry and present our results. In Section 6, we quantify the sensitivity of the derived mass-loss rates to various systematic effects. In Section 7, we discuss the implications of our results.

2 THE SAMPLE AND DATA

With the advent of *Spitzer*, well-calibrated mid-IR observations of the Magellanic Clouds became available, thanks to the *Spitzer* SAGE legacy data products provided by Meixner et al. (2006) for the LMC and Gordon et al. (2011) for the SMC. These data present the opportunity to obtain a large, uniform set of IR derived mass-loss rates from lightly reddened stars, with well-determined luminosities. Bonanos et al. (2009, 2010) took advantage of the new data and compiled catalogues by starting with all massive stars in the LMC and SMC with high-quality spectral classifications, and then matching them to entries in the *Spitzer* and other photometric data bases. The catalogues contain *U*, *B*, *V* and *I* from various sources and *JHK* photometry (primarily from the Two-Micron All Sky Survey, 2MASS; Skrutskie et al. 2006) and the targeted IRSF survey,

(Kato et al. 2007), together with *Spitzer* IRAC [3.6], [4.5], [5.8] and [8.0] photometry and some MIPS [24] photometry (see Bonanos et al. for details). The Bonanos et al. catalogues contain 341 LMC and 195 SMC O stars with high-quality spectral types and optical, NIR and *Spitzer* mid-IR photometry through [4.5]. Bonanos et al. also demonstrated that the O stars had detectable IR excesses due to winds, but did not perform a quantitative analysis of individual stars.

In this paper, we concentrate on a sub-sample of the Bonanos et al. (2009, 2010) catalogues, namely those O stars which are also in the Blair et al. (2009) *FUSE* sample. This will allow direct comparison of results derived from different diagnostics in many cases. We rejected stars later than B0, since their winds can contain a significant fraction of neutral hydrogen. This fraction can be strongly dependent upon non-local thermodynamic equilibrium (NLTE) processes and clumping in the wind, both of which introduce unwanted complications into the modelling (see Petrov et al. 2014). We also rejected WR stars since their massive winds require a full treatment of electron scattering, which we neglect. After imposing these restrictions, our sample contained 46 SMC and 58 LMC O stars (see Tables 1 and 2).

We supplemented the CCD based optical photometry listed by Bonanos et al. with photoelectric *V* and *B* photometry from the literature whenever possible and assigned errors of 0.03 mag to each. Priority was given to the photoelectric photometry. We eliminated the *Spitzer* MIPS data, since very few stars were detected at [24]. The *I*-band photometry was also eliminated for reasons discussed in Section 4.1, and *U*-band photometry was not included since CCD *U*-band photometry (which is all that exists for most of the stars) often has calibration issues and it was not needed for our purposes.

The Bonanos et al. (2009) calibrations and effective wavelengths were used, with two exceptions. First, the Kato et al. (2007) IRSF to 2MASS conversion factors were applied to the IRSF photometry. Secondly, the *B*-band zero magnitude flux was decreased by 4 per cent with respect to the one listed by Bonanos et al.. This was needed to produce $(B - V)$ indices that agree with the Fitzpatrick & Massa (2005) calibration and to ensure that derived $E(B - V)$ values are greater than 0.

3 STELLAR PARAMETERS AND REDDENING

To determine the underlying photospheric flux of each program star and its expected theoretical mass-loss rate, we must know its physical parameters, i.e. mass, effective temperature, luminosity and chemical composition. We obtain these from the SMC and LMC spectral type to luminosity, effective temperature and mass calibrations provided by Weidner & Vink (2010). Tables 1 and 2 summarize the physical parameters for the SMC and LMC samples, respectively. We used the spectral types from the Bonanos et al. catalogues for most stars, and exceptions are noted in the tables.

Observed colour excesses, $E(B - V)_{\text{obs}}$, were determined using $(B - V)_0$ values from TLUSTY model atmospheres (Lanz & Hubeny 2003) with the appropriate T_{eff} , $\log g$ and metallicity. These same models were used to determine the photospheric fluxes of the stars.

To characterize the optical and IR extinction, we adopt the Weingartner & Draine (2001) curves for the SMC and LMC. As with all other wavelength ranges, the form of the IR extinction law is variable (e.g. Fitzpatrick & Massa 2009; Schlafly et al. 2016). However, because reddening is minimal in most cases, the exact form of the extinction curve used is not too important. Nevertheless, the effects of variations in $R(V) \equiv A(V)/E(B - V)$ are taken into account by allowing $E(B - V)$ to be a free parameter in fitting the IR continua

Table 1. SMC stellar properties. (Full table is available online.)

Name	Spectral type	Reference	V	$(B - V)$	T_{eff}	$\log L/L_{\odot}$	M/M_{\odot}	R/R_{\odot}
AzV14	O3-4 V	B10	13.77	-0.19	44 338	5.44	44.35	8.91
AzV435	O4 V	B10	14.13	-0.07	43 292	5.40	41.15	8.88
AzV177	O4 V	B10	14.53	-0.21	43 292	5.40	41.15	8.88
NGC346-007	O4 V(f+)	B10	14.02	-0.24	43 292	5.40	41.15	8.88
AzV75	O5 I(f+)	B10	12.79	-0.16	38 715	5.81	54.79	17.76

Note. B10: Bonanos et al. 2010; P09: Penny & Gies (2009); M95: Massey et al. (1995).

Table 2. LMC stellar properties. (Full table is available online.)

Name	Spectral type	Reference	V	$(B - V)$	T_{eff}	$\log L/L_{\odot}$	M/M_{\odot}	R/R_{\odot}
Sk -66° 172	O2 III(f*)+OB	B09	13.13	-0.12	48 849	5.93	84.09	12.92
Sk -68° 137	O2 III(f*)	B09	13.35	-0.08	48 849	5.93	84.09	12.92
LH64-16	ON2 III(f*)	B09	13.67	-0.22	48 849	5.93	84.09	12.92
Sk -70° 91	O2 III	B09	12.78	-0.23	48 849	5.93	84.09	12.92
BI 237	O2 V((f*))	B09	13.98	-0.12	51 269	5.82	79.66	10.24

Note. B09: Bonanos et al. (2009); and P09: Penny & Gies (2009).

(see Section 5). The consequences of this action are examined in Section 6.

4 THE WIND MODEL

4.1 Formulation of the model

In general, the wind density of a smooth spherically symmetric flow from a star of radius R_* is determined by the wind velocity law and the mass-loss rate, \dot{M} . Typically, the velocity law for a wind with a terminal velocity v_{∞} is assumed to have the form

$$w = \left(1 - \frac{a}{x}\right)^{\beta}, \quad (1)$$

where $w = v/v_{\infty}$, $x = r/R_*$, $a = 1 - w_0^{1/\beta}$ and $w_0 = w(x=1)$. These wind laws have a maximum velocity gradient at $x = 1$, and laws with larger β parameters accelerate more slowly. In the following, we adopt $\beta = 1$ and $w_0 = 0.01$, which are typical values for OB stars. Whenever possible, v_{∞} values derived from UV observations were collected from the literature. If none were available, we derived v_{∞} from the stellar parameters and the prescription provided by Vink, de Koter & Lamers (2001). Their method was also used to calculate theoretical mass-loss rates, $\dot{M}(\text{Vink})$. The mass-loss rates derived from IR excesses turn out to be more sensitive to the wind parameters than the stellar parameters.

The continuity equation relates the wind density and the velocity

$$\rho = \frac{\dot{M}}{4\pi R_*^2 v_{\infty} x^2 w(x)}. \quad (2)$$

Thus, ρ varies rapidly as x approaches 1; is proportional to \dot{M} ; is inversely proportional to v_{∞} ; and, is denser at a given x for larger β . The IR emission from a wind is dominated by free-free and free-bound emission and absorption by H and He. It can originate very near the star (the exact radius depends upon wavelength and wind density).

Because our goal is to survey several objects in order to determine mean properties, identify outliers, contrast differences between the LMC and SMC, compare the results with theoretical expectations, and search for trends. To accomplish this, we model the observed IR excesses of 104 O stars. Consequently, we sought the simplest

available model that captures the essential physics of IR continuum formation. A computational fast model that suffers only a minimal loss of precision is the one developed by Lamers & Waters (1984a,b, hereafter **LWa** and **LWb**). This is a core-halo model wherein the flux from a static plane parallel model atmosphere is embedded in a stellar wind and both the emission and absorption by the wind material are treated in detail. As is typical, the wind is assumed to be uniform and spherically symmetric with a density structure set by the velocity law. For simplicity, it is also assumed that the wind is in LTE at a fixed temperature, T_w , typically $0.8-0.9 \times T_{\text{eff}}$.

We employ the **LWa** model together with **TLUSTY** models (with appropriate SMC or LMC metallicities) for the underlying photospheres. In this core-halo formulation, the observed flux, $f(\lambda)$, and the flux of the underlying photosphere, $f(\lambda)_p$, are related by

$$f(\lambda) = \left[Z(\lambda)_1 + Z(\lambda)_2 \frac{f(\lambda)_w}{f(\lambda)_p} \right] f(\lambda)_p, \quad (3)$$

where $f(\lambda)_w$ is a Planck function with $T = T_w$ and Z_1 and Z_2 are functions that represent the attenuation of the stellar flux by the wind and the emission and self-absorption of the wind, respectively. These functions are integrals over the impact parameter, q , and can be calculated very quickly once the optical depth through the wind as a function of impact parameter, $\tau(q)$, is known. While determining $\tau(q)$ can be time consuming, it only has to be done once for a given set of wind law parameters, β and w_0 . Consequently, tables of $\tau(q)$ as a function of q can be constructed for each velocity law and then scaled by the mass-loss rate, terminal velocity and T_w . These can be integrated very quickly over q to obtain a specific model.

When fitting the models to the observations, we use a version of equation (3) that is normalized to the flux at V and accounts for extinction, viz,

$$\frac{f(\lambda)}{f(V)} = \frac{[Z(\lambda)_1 + Z(\lambda)_2 f(\lambda)_w/f(\lambda)_p] f(\lambda)_p 10^{-0.4A(\lambda)}}{[Z(V)_1 + Z(V)_2 f(V)_w/f(V)_p] f(V)_p 10^{-0.4A(V)}}, \quad (4)$$

where $f(\lambda)_p$ is a **TLUSTY** model, which depends on T_{eff} , $\log g$ and metallicity, and $Z_1(\lambda)$ and $Z_2(\lambda)$ depend on the velocity-law parameters, β , w_0 and v_{∞} and \dot{M} . We also assume that $Z(V)_1 = 1$ and $Z(V)_2 = 0$, which gives

$$\frac{f(\lambda)}{f(V)} = \left[Z(\lambda)_1 + Z(\lambda)_2 \frac{f(\lambda)_w}{f(\lambda)_p} \right] \frac{f(\lambda)_p}{f(V)_p} 10^{-0.4E(\lambda-V)}. \quad (5)$$

In performing the fits, we adopt a logarithmic version of this equation,

$$\log \frac{f(\lambda)/f(V)}{f(\lambda)_p/f(V)_p} = \log \left[Z(\lambda)_1 + Z(\lambda)_2 \frac{f(\lambda)_w}{f(\lambda)_p} \right] - 0.4E(B - V)k(\lambda - V), \quad (6)$$

where $k(\lambda - V) \equiv E(\lambda - V)/E(B - V)$, so $E(\lambda - V) = E(B - V)k(\lambda - V)$. Note that $k(\lambda - V) < 0$ for $\lambda > \lambda_V$.

Following **LW**a, we do not extend the wind model to wavelengths shorter than $1 \mu\text{m}$. Shorter wavelengths require including the Paschen jump at $0.82 \mu\text{m}$. This could introduce sizable uncertainties. The strength of the Paschen jump is much stronger than the Brackett jump (at $1.46 \mu\text{m}$) because the populations of the Hydrogen levels increase dramatically with decreasing quantum number. Further, the populations of the lower hydrogen levels are strongly affected by NLTE effects, so the exact strength of the jump cannot be accurately predicted by the LTE assumption of the **LW**a model. As a result, we bypass the problem by not including *I*-band photometry in the fits, which is the only filter strongly affected. In addition, available *I*-band calibrations are not very reliable (see Fitzpatrick & Massa 2005).

Because the **LW**a core–halo models can be calculated almost instantaneously, they are ideal for the current work because we use a non-linear least-squares fitting routine, where each fit typically involves several tens of model calculations, and this has to be done for 104 stars. In addition, we also examine how a variety of constraints and systematic errors affect the results, a feat that would be extremely time consuming for more sophisticated models. We also ignore the effects of electron scattering, but this should be a minor effect for the stars and wavelengths considered here.

A final simplification used to increase calculation speed was to apply a photometric calibration based on effective wavelength, λ_{eff} . We tested the validity of this approach by comparing the fluxes derived this way to those determined from integrating over filter response curves. Over the small range of intrinsic colours and colour excesses in the current sample, the effects were all less than 1 per cent.

4.2 Accuracy of the model

To determine the accuracy of the mass-loss rates determined by the simple **LW**a model, we performed the following experiment. We employed the unclumped CMFGEN models calculated by Martins & Plez (2006) as surrogates for actual stars. These were then fitted with **LW**a models, using equation (6). To begin, we constructed a set of Galactic abundance **TUSTY** models whose T_{eff} and $\log g$ values correspond to the CMFGEN models. For the **LW**a models, we used $\beta = 0.9$ (same as the CMFGEN models used) and assumed $w_0 = 0.01$ since, unlike the CMFGEN models, the **LW**a models do not continue into the photosphere. We set $T_w = 0.9 T_{\text{eff}}$, since this gave the best overall agreement. The near equality of the wind and stellar temperatures is reasonable since, at the wavelengths considered here, the bulk of the wind emission comes from very near the stellar surface. The fits also allowed for reddening to be present as well, using a Weingartner & Draine (2001) $R(V) = 3.1$ extinction curve. This simulates fitting actual data, since any difference between the **LW**a models and the CMFGEN models which has a wavelength dependence similar to an extinction curve will be absorbed into the measured extinction. We also allowed for a 2 per cent error in each point, to simulate photometric errors.

All of the fits were excellent, with reduced $\chi^2 < 1$. A few aspects of the fits are noteworthy. First, two models ($T_{\text{eff}} = 32\,500\text{ K}$,

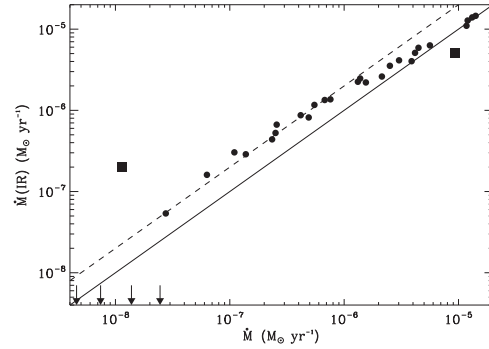


Figure 1. Mass-loss rates (in $M_{\odot} \text{ yr}^{-1}$) determined from **LW**a model fits to the IR continua of the CMFGEN models of Martins & Plez (2006), $\dot{M}(\text{IR})$, versus the CMFGEN model mass-loss rates, \dot{M} . The points shown as squares are for CMFGEN models whose fluxes deviate from the trends of models with similar physical parameters. The upper limits are for models where the fit could not determine a significant \dot{M} , when photometric errors of 0.02 mag are assigned to each photometry point. The solid line is $\dot{M} = \dot{M}(\text{IR})$, and the dashed line is $\dot{M} = 2 \dot{M}(\text{IR})$. Overall, the mass-loss rates determined by the simple **LW**a models recover the CMFGEN rates very well for high mass-loss rates, but then begin to overestimate the mass-loss rates for models with smaller \dot{M} . Even so, the disagreement is typically within a factor of 2 for cases where mass-loss rates are detectable.

$\dot{M} \times 10^6 = 0.011$ and $T_{\text{eff}} = 37\,500\text{ K}$, $\dot{M} \times 10^6 = 9.33$) do not fit the trends defined by models with similar parameters. The reason for this discord is unknown. Secondly, very few of the $E(B - V)$ values derived from the fits are larger than 0.01 mag, implying that the model distinguishes between reddening and wind excesses very well. Thirdly, some CMFGEN models with very low mass-loss rates have IR continua that are *fainter* than the corresponding **TUSTY** model, resulting in small ‘negative excesses’, which resulted in negative $E(B - V)$ values. This effect is likely related to differences in the structure of the outer atmospheres of the CMFGEN and **TUSTY** models caused by including the dynamic nature of the outer atmosphere in the CMFGEN models. While interesting, this effect is very small, with the magnitude of the negative excesses always less than 0.01 mag.

Fig. 1 summarizes the comparison of the two models. It shows the mass-loss rate derived from the **LW**a model that provides the best fit to the IR continuum of the CMFGEN model, $\dot{M}(\text{IR})$, versus the CMFGEN \dot{M} values. The $\dot{M}(\text{IR})$ values are nearly identical to the CMFGEN \dot{M} values for models with large mass-loss rates. For $\dot{M} \lesssim 2 \times 10^{-6} M_{\odot} \text{ yr}^{-1}$, the $\dot{M}(\text{IR})$ values overestimate the CMFGEN \dot{M} values by about a factor of 2. Finally, for the smallest \dot{M} values, the fitting cannot detect a significant excess, resulting in $\dot{M}(\text{IR}) \simeq 0$.

The significant result of this exercise if we assume that the CMFGEN models provide a good representation of the IR continua of real stars, then the simple **LW**a core–halo model faithfully represents actual IR continua. Further, fitting IR continua with the **LW**a model results in $\dot{M}(\text{IR})$ values that are very accurate for stars with $\dot{M} \gtrsim 2 \times 10^{-6} M_{\odot} \text{ yr}^{-1}$, but may overestimate the actual \dot{M} values by a factor of 2 for $\dot{M} \lesssim 2 \times 10^{-6} M_{\odot} \text{ yr}^{-1}$.

5 RESULTS

To summarize, the following ingredients are used in the fits: Weidner & Vink (2010) tables to translate spectral types into physical parameters; **TUSTY** models with these parameters to give the photospheric fluxes; and, Weingartner & Draine (2001) extinction curves

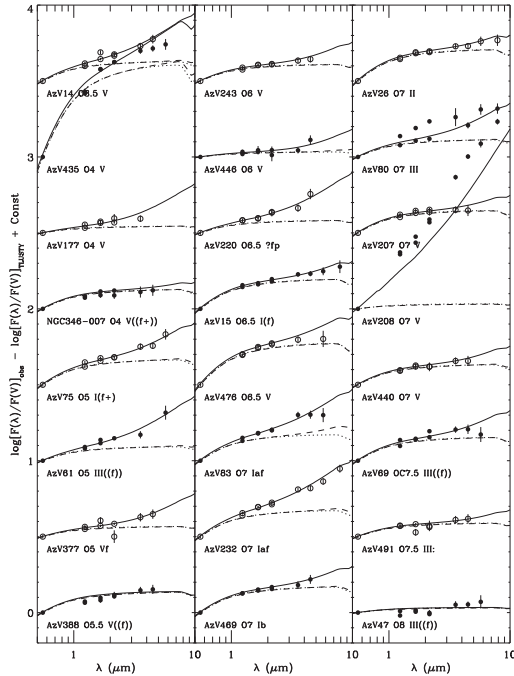


Figure 2. Each plot shows a model fit to the log of the fluxes minus the log of the appropriate *TLUSTY* model, both normalized to *V*. For each star, the observed data are shown as points, with every other curve shown as open or filled points to avoid confusion when points of adjoining SEDs overlap. The black curve is the model fit, the dotted curve shows the reddening determined by the fit, and the dashed curve is the reddening plus the excess expected from the Vink et al. (2001) mass-loss rate, $\dot{M}(\text{Vink})$. One σ errors (often smaller than the points) are shown and successive curves are offset by 0.5 dex from the bottom for display.

to characterize the extinction. We examine the implications of these assumptions in Section 6.

For each star, the observed and *TLUSTY* SEDs were normalized by their *V*-band fluxes. The difference, $\log f(\lambda)/f(V) - \log f(\lambda)_p/f(V)_p$, is the IR excess. This excess was fit using equation(6) and a non-linear least-squares routine to determine two free parameters: $\dot{M}(\text{IR})$, which is the mass-loss rate of the best-fitting *LW*a model, and $E(B - V)$ [or, equivalently, $R(V)$, see Section 6].

Figs 2 and 3 show the SMC fits, Figs 4–6 show the LMC fits, and Tables 3 and 4 list the results. Because these figures show the differences between the log of the observed fluxes and the appropriate *TLUSTY* model, any shape is due to either reddening or wind excess. The photometry is shown as filled or open points and the best-fitting model for each star is shown as a thick black curve. The excess that would result from the derived reddening and the excess expected from the mass-loss rate predicted using the Vink et al. (2001) formulae, $\dot{M}(\text{Vink})$, is shown as the dashed curve. The contribution of reddening to the fits is shown as a dotted curve (not always visible because it often coincides with the dashed curve). For each star, the difference between the dotted curve and the black curve is the IR excess, and the difference between the dashed curve and the black curve is the excess over the IR continuum expected for $\dot{M}(\text{Vink})$. A few stars, such as AzV 47, show little evidence of either wind excess or reddening. Several, such as AzV 120 and AzV 216, are well fitted by reddening alone. For most stars, there is a clear excess relative to pure extinction and to the $\dot{M}(\text{Vink})$ curves.

In general, the fits in Figs 2–6 are quite good. However, four stars: Az V207, AzV 461, NGC346-026 and AzV 235, have ex-

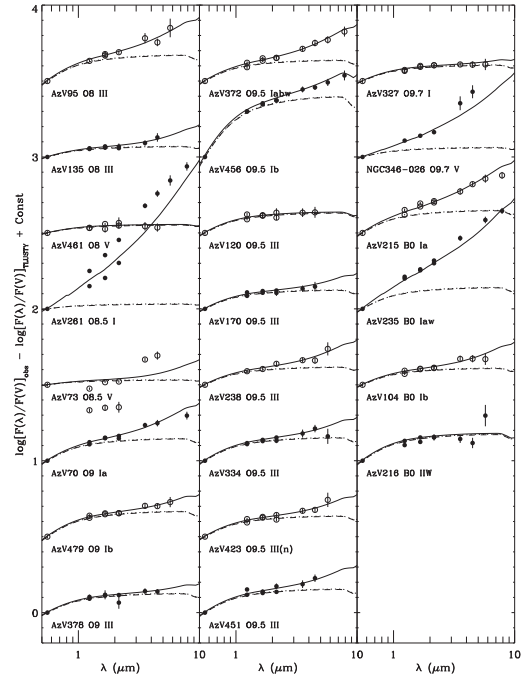


Figure 3. Same as Fig. 2.

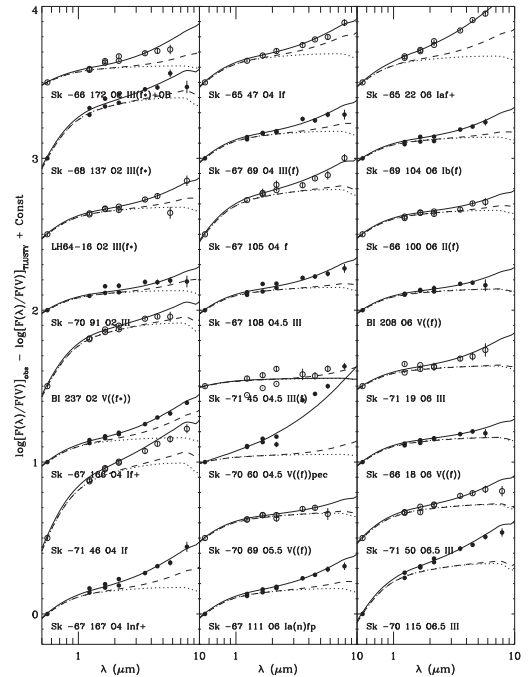


Figure 4. Same as Fig. 2 for the LMC sample.

remely large excesses and are poorly fit. The $\dot{M}(\text{IR})$ for these stars are unreliable since their huge excesses suggest circumstellar discs (see fig. 10 in Bonanos et al. 2010). Consequently, stars with $\dot{M}(\text{IR})/\dot{M}(\text{Vink}) > 100$ (more than twice the next largest ratio) are identified as probable discs systems in Table 3 (all are in the SMC). Notice too, that there is evidence that the IR fluxes varied for some stars with large excesses. For example, the two sets of nearly parallel, but off set, points for AzV 243 are from the two *JHK* surveys, which were obtained at different epochs.

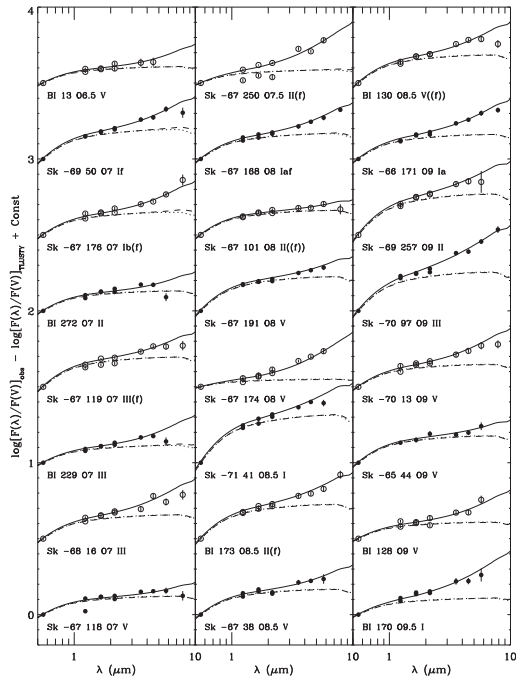


Figure 5. Same as Fig. 4.

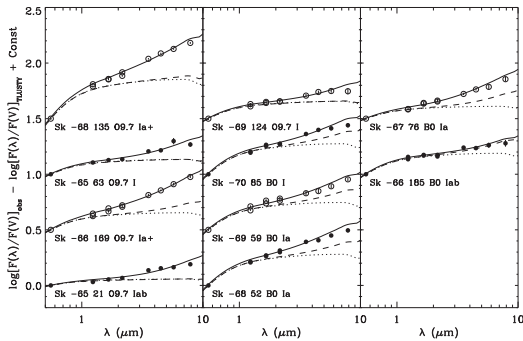


Figure 6. Same as Fig. 4.

A few other properties of the SEDs are also noteworthy. For example, the SEDs of a few stars, such as AzV435 and Sk-71°46, show the effects of relatively large reddening. It is also interesting to contrast the excesses and $\dot{M}(\text{IR})$ values of the O2 star Sk -70°90 and the O4.5 star Sk -67°108. The former has a smaller excess, but a larger $\dot{M}(\text{IR})$. This is because the O2 star has a much larger v_∞ , so the wind density (and IR emission) is lower for the same $\dot{M}(\text{IR})$.

While the fits for most stars shown in Figs 2–6 appear to have distinct IR excesses, the evidence is marginal in some cases (e.g. AzV69, AzV135, BI 208 and Sk -67°118). This is an important point since even a small IR excess can imply a fairly large $\dot{M}(\text{IR})$, $\sim 10^{-6} M_\odot \text{ yr}^{-1}$, which can be far larger than expected. To address this problem, all of the stars were fitted a second time, with $E(B - V)$ as the only free parameter and $\dot{M}(\text{IR})$ set to 0. We then formed the ratio of the χ^2 s for the fits with and without mass-loss and compared them to an F -distribution. Stars whose ratios correspond to a 50 per cent or more probability of being drawn from the same distribution are flagged in Tables 3 and 4, since there is a good chance that they have no detectable mass-loss.

Tables 3 and 4 contain several stars whose fits result in relatively large χ^2 . Ignoring the probable discs, an inspection of Figs 2–(6) reveals that nearly all of the fits with $\chi^2 \geq 4$ are due to a large discrepancy in the two sets of JHK photometry. This means that either the photometry errors are incorrect, or that the JHK fluxes are variable. Whatever the case, the fits tend to go through the mean of the two sets and usually fit the mid-IR quite well. Since it is the *Spitzer* fluxes that determine $\dot{M}(\text{IR})$, we believe that most of these fits are better than their χ^2 would indicate. However, there are two cases that cannot be explained as a discordant NIR photometry. One is AzV 388, whose continuum seems to have a distinctly different shape than expected, for reasons that are not clear. The other is AzV 435, whose derived $E(B - V)$ is the largest of the entire sample. Further, it has largest difference between $E(B - V)$ and $E(B - V)_{\text{obs}}$, suggesting a peculiar extinction curve, whose shape may be very different from the one used in the fitting, resulting in a poor fit. This case illustrates the difficulties encountered when fitting the IR continua of heavily reddened stars.

Fig. 7 shows the ratio of the derived $\dot{M}(\text{IR})$ divided by $\dot{M}(\text{Vink})$ for all of the program stars plotted against $\dot{M}(\text{Vink})$. The red symbols are for LMC stars and the black symbols are for SMC stars. The downward pointing arrows indicate stars whose best fits implied $\dot{M}(\text{IR})=0$, stars with a 50 per cent or more probability of having no wind are shown as open symbols, and stars whose fits had a $\chi^2 \geq 4$ are shown as crosses. Two aspects of Fig. 7 are worth noting. The first is that for $\dot{M}(\text{Vink}) \gtrsim 10^{-6} M_\odot \text{ yr}^{-1}$, the relation between the observed and expected mass-loss rates tightens, and $\dot{M}(\text{IR}) \simeq 2 \dot{M}(\text{Vink})$. The second is that for $\dot{M}(\text{Vink}) \lesssim 10^{-7} M_\odot \text{ yr}^{-1}$, even when the non-detections, probable non-detections and stars with obvious discs are ignored, more than half of the stars still have solid detections, implying that the large measured excesses are quite real.

6 SYSTEMATIC EFFECTS

This section examines how the derived mass-loss rates are affected by errors in: spectral classifications; the neglect of wind emission

Table 3. SMC Wind Properties. (Full table is available online.)

Name	v_∞ (km s $^{-1}$)	Reference	$\dot{M}(\text{Vink})$ ($10^{-6} M_\odot \text{ yr}^{-1}$)	$\dot{M}(\text{IR})$	$E(B - V)$ (mag)	$E(B - V)_{\text{obs}}$	χ^2
AzV14	2000	M04	0.40	4.22 ± 0.75	0.12 ± 0.013	0.16	1.84
AzV435	1500	M07	0.48	3.20 ± 0.50	0.55 ± 0.013	0.27	6.09
AzV177	2650	M05	0.24	4.39 ± 0.88	0.04 ± 0.009	0.13	3.49
NGC 346-007	2300	M07	0.28	0.91 ± 1.21	0.12 ± 0.006	0.10	1.53
AzV75	2100	M07	1.10	8.73 ± 1.25	0.15 ± 0.008	0.16	0.96

* – Consistent with no wind; D – probable disc; v_∞ are theoretical values.

Notes. E04: Evans et al. (2004); M04: Massey et al. (2004); M05: Massey et al. (2005); M09: Massey et al. (2009); M07: Mokiem et al. (2007); P96: Puls et al. (1996); and VVV: Vink et al. (2001).

Table 4. LMC wind Properties. (Full table is available online.)

Name	v_∞ (km s ⁻¹)	Reference	$\dot{M}(\text{Vink})$ (10 ⁻⁶ M _⊙ yr ⁻¹)	$\dot{M}(\text{IR})$ (10 ⁻⁶ M _⊙ yr ⁻¹)	$E(B - V)$	$E(B - V)_{\text{obs}}$ (mag)	χ^2
Sk -66°172	3100	C16	3.19	9.16 ± 0.99	0.11 ± 0.007	0.23	3.33
Sk -68°137	3400	C16	2.84	7.17 ± 0.83	0.39 ± 0.005	0.27	6.58
LH64-16	3250	C16	3.01	6.35 ± 0.82	0.18 ± 0.005	0.13	2.05
Sk -70°91	3150	C16	3.12	4.90 ± 0.73	0.13 ± 0.005	0.12	2.48
BI 237	3400	C16	1.85	3.88 ± 0.58	0.41 ± 0.005	0.24	1.12

Notes. C16: Crowther et al. (2016); and VVV: Vink et al. (2001).

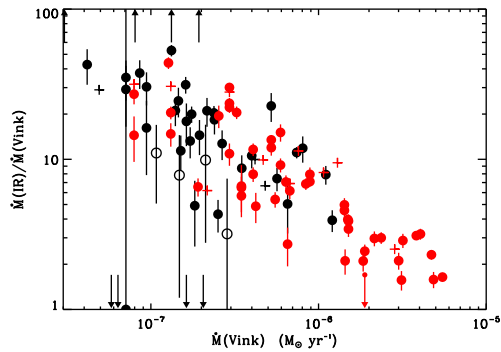


Figure 7. Ratios of the mass-loss rates determined from IR excesses, $\dot{M}(\text{IR})$, to the theoretical mass-loss rates, $\dot{M}(\text{Vink})$, versus $\dot{M}(\text{Vink})$. Red and black points are for the LMC and SMC samples, respectively. Open circles represent stars whose measured $\dot{M}(\text{IR})$ values are consistent with zero, downward arrows are for stars whose best fits give $\dot{M}(\text{IR}) = 0$, crosses are for stars with reduced $\chi^2 > 4$ and upward arrows are for stars with very large mass-loss rates, probably from discs.

on the B and V photometry; variations in the extinction curves; the assumed wind temperature; and, the velocity law parameters.

Changing the spectral and luminosity classes (and, hence, the stellar parameters) changes $f(\lambda)_p$ and $\dot{M}(\text{Vink})$. Nevertheless, simulations showed that the derived $\dot{M}(\text{IR})$ were not very sensitive to classification errors of ± 1 spectral or luminosity class and changed by less than 20 per cent in both cases.

Comparisons to CMFGEN models (Section 4.1), suggest that our assumption that B and V are unaffected by wind emission is reasonable in most cases. However, in the few instances where the wind emission is strong enough to affect the optical photometry, it will contaminate V more than B . This creates an intrinsic $E(B - V)$, causing an over correction for extinction, which, in turn, leaves less excess to be accounted for by $\dot{M}(\text{IR})$, resulting in an underestimate of $\dot{M}(\text{IR})$. Since our major concern is effects that might lead us to overestimate $\dot{M}(\text{IR})$, this issue is not considered further.

Variations in the extinction law are another concern. Fig. 8 demonstrates how changing $E(B - V)$ or $R(V)$ are equivalent over the wavelength range of interest. It shows two Weingartner & Draine (2001) Galactic curves: one for $R(V) = 3.1$ and one for $R(V) = 5.5$ divided by 1.7. The locations of the photometric bands are also indicated. The figure shows that for wavelengths longer than V , rescaling an extinction curve with one value of $R(V)$ results in a good approximation of an extinction curve with a different $R(V)$. However, for large values of $E(B - V)$, the differences can become important, introducing errors of 0.1 mag or more. That is why it is best to derive IR excesses for stars with small colour excesses.

The degeneracy of $E(B - V)$ and $R(V)$ was the motivation for allowing $E(B - V)$ to be a free parameter when fitting the SEDs

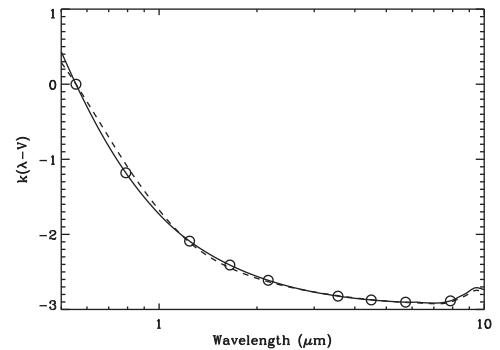


Figure 8. Comparison of Weingartner & Draine (2001) extinction curves for $R(V) = 3.1$ (black curve) and $R(V) = 5.5$ (dashed curve). The $R(V) = 5.5$ has been divided by 1.7 to demonstrate how very different curves can appear proportional for wavelengths longer than V .

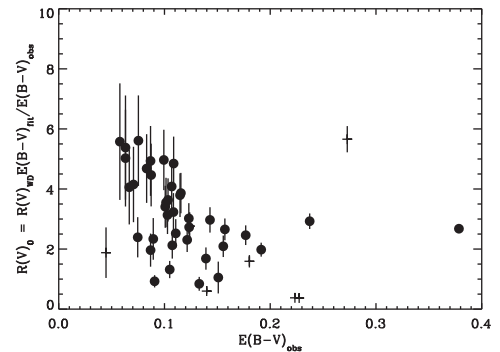


Figure 9. Values of $R(V)$ derived from the fits plotted against $E(B - V)_{\text{obs}}$ for the SMC sample. Solid points have a reduced $\chi^2 < 4$ and crosses have $\chi^2 \geq 4$. The plot suggests a foreground contribution to the extinction of $E(B - V) \simeq 0.05$ mag from dust with a rather large $R(V)$, which then melds into SMC dust with a much smaller $R(V)$. Both components may be rather patchy, accounting for the large scatter.

instead of simply setting it equal to $E(B - V)_{\text{obs}}$. This accommodates possible variations in $R(V)$. If the actual value of $R(V)$ along the line of sight, $R(V)_0$, differs from the assumed Weingartner & Draine (2001) value, $R(V)_{\text{WD}}$, then it should be possible to recover $R(V)_0$, from the relation

$$E(B - V)_{\text{obs}} R(V)_{\text{WD}} = E(B - V)_{\text{fit}} R(V)_0, \quad (7)$$

where $E(B - V)_{\text{fit}}$ is the excess obtained from the fit. Fig. 9 shows $R(V)_0$ plotted against $E(B - V)_{\text{obs}}$ for the SMC sample. Considering that all of the excesses are small and that the errors are large, we see

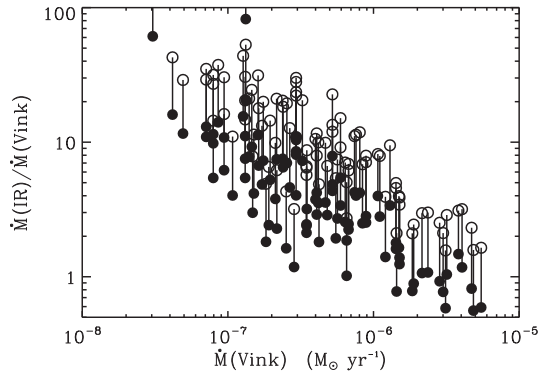


Figure 10. The effect of changing β on the derived mass-loss rates for the sample shown in Fig. 7. The plot shows $\dot{M}(\text{IR})/\dot{M}(\text{Vink})$ as a function of $\dot{M}(\text{Vink})$. Open points are $\dot{M}(\text{IR})$ derived using $\beta = 1$, filled points are $\dot{M}(\text{IR})$ derived using $\beta = 2.5$, and lines connect points for the same star.

that there is a general trend for $R(V)_0$ to decrease with increasing $E(B - V)_{\text{obs}}$. This is consistent with the sight lines passing through a small amount of foreground, Galactic dust, with an $R(V) \sim 4$ and then passing through more and more SMC dust with $R(V) \sim 2.5$. Although the line of sight to the SMC was not included in Schlafly et al. (2017), they do detect $R(V) \sim 4$ for high-latitude Galactic dust in nearby fields. Further, $R(V) \sim 2.5$ is consistent with the SMC $R(V)$ determined by Gordon & Clayton (1998). Keeping in mind that neither the foreground nor the SMC dust are probably perfectly uniform, the general trend appears to verify our assumption that the value of $R(V)$ is changing from one line of sight to the next, and the amount of change depends on the relative amounts of the Galactic and the SMC dust encountered.

Assigning an incorrect temperature to the wind can affect the results. The wind temperature could be much higher than $0.9T_{\text{eff}}$ if shocks and their associated X-rays heat the wind to temperatures $\sim 10^6$ K, as suggested by Cassinelli et al. (2001). However, increasing T_w to 10^6 K only reduces $\dot{M}(\text{IR})$ by 30 per cent.

Finally, we examined how changing the parameters in the velocity law, equation (1), affects the derived mass-loss rates. Changing w_0 over the range of $0.005 \leq w_0 \leq 0.02$ (the most commonly used values) changed the derived $\dot{M}(\text{IR})$ values by 20 per cent or less, which is small compared to the observed disagreement between theory and observation.

It is particularly important to examine the effect of changing v_{∞} for the less luminous stars. For most of these stars, observed values are not available so we rely on the values predicted by Vink et al. (2001). When observed values are available, they are often much less than the predicted ones, but this could be a systematic effect. It is difficult to measure v_{∞} in less luminous stars, since their wind lines are typically asymmetric, lacking a distinctive blue edge. This makes the full extent of the wind absorption hard to measure and easy to underestimate. However, experiments show that reducing v_{∞} by a factor of 2 reduces $\dot{M}(\text{IR})$ by 40 per cent. While substantial, this is too little to explain the observed $\dot{M}(\text{IR})/\dot{M}(\text{Vink})$ ratios.

In contrast to the other parameters, β can have a major effect on the derived $\dot{M}(\text{IR})$ values (as noted by LWa). Changing β from 1 to 2.5 reduces the inferred \dot{M} by a factor of 2.7. Fig. 10 demonstrates this effect. It arises because a larger β reduces the velocity gradient (increasing the density) near the surface of the star, where most of the emission occurs. We return to this issue in the next section.

7 DISCUSSION

Our results can be summarized as follows: Mass-loss rates determined from IR excesses are larger than expected, increasing from about a factor of 2 for the most luminous stars to about 40 for the least luminous stars with detectable IR excesses; and, the LMC and the SMC results are similar. Because we have shown that $\dot{M}(\text{IR})$ derived by the LWa models can overestimate the actual \dot{M} by a factor of 2 for stars with $\dot{M} \lesssim 2 \times 10^{-6} M_{\odot} \text{ yr}^{-1}$, these results are consistent with $\dot{M}(\text{Vink}) \lesssim \dot{M}(\text{IR}) \lesssim 2\dot{M}(\text{Vink})$ for $\dot{M}(\text{Vink}) \gtrsim 2 \times 10^{-6} M_{\odot} \text{ yr}^{-1}$, growing to $5\dot{M}(\text{Vink}) \lesssim \dot{M}(\text{IR}) \lesssim 20\dot{M}(\text{Vink})$ for the least luminous stars. Thus, if we interpret the IR excesses in terms of mass-loss, they infer rates that are equal to or much larger than theoretical predictions. This is in stark contrast to recent mass-loss rates determined from UV wind lines, H α and X-ray diagnostics, which suggest rates smaller than the Vink et al. (2001) predictions by a factor of 2 to 3 (see Martins & Palacios 2017 for a summary).

However, it is well known that increasing the mass-loss rate is not the only way to increase the IR emission. In this section, we argue that the large IR excesses and their implied large $\dot{M}(\text{IR})$ values are not the result of large mass-loss rates. Instead, we attribute them to density and velocity structures near the base of the wind. We also consider the implications of the scatter in Fig. 7 and the fact that points from stars in both galaxies are interspersed.

Throughout the discussion, we emphasize that the IR excesses in our sample originate very near the stellar surface. To see this, consider the effective radii of the IR excesses. Using a $\beta = 1$ velocity law and our longest wavelength, $8.0 \mu\text{m}$, even the strongest winds in our sample (aside from the obvious discs) result in a value of the LWa parameter E_v (their equation 6) that is less than 0.01. This implies an effective radius that is only a few per cent larger than the stellar radius (see LWa Fig. 4).

At O star temperatures, the intensity of the IR wind emission is proportional to the density squared, and there are two ways to enhance this for a fixed mass-loss rate. One is to collect most of the wind mass into structures or clumps with enhanced densities. The other is to reduce the velocity gradient, which then increases the density through the continuity equation. Since, as outlined in Section 1, evidence for structure in O star winds abounds, including indications that this structure originates near the stellar surface, we suspect that this structure accounts for much of the large excesses. The notion that we are seeing effects that originate near the stellar surface is reinforced by the fact that the largest discrepancies occur for stars with lower expected mass-loss rates, where we expect to see nearly to the stellar surface.

It is possible to make our results a bit more quantitative. First, consider the case where all of the excess is due to density inhomogeneities. Abbott, Biegging & Churchwell (1981) developed a simple model for how clumping enhances the observed emission. It assumes that the wind consists of two components whose density ratio is x , where $0 \leq x \leq 1$, and the fraction of the wind volume occupied by the higher density is f_v . The geometry of the structures is unspecified. Setting $x = 0$ gives the largest enhancements for fixed f_v , with the ratio of the observed to actual mass-loss rates being simply $f_v^{-1/2}$. In our case, this ratio is $\dot{M}(\text{IR})/\dot{M}(\text{Vink})$. For stars with smaller $\dot{M}(\text{Vink})$, this ratio varies between 5 and 20 (where an overestimate of 2 by $\dot{M}(\text{IR})$ is assumed). Thus, if the entire discrepancy is attributed to clumping, stars with weak winds must have all of the wind material confined to between 0.3 and 4 per cent of the wind volume. This is in contrast to stars with more massive the winds, where Massa & Prinja (2015) showed that the wind

structures near the photosphere are quite large and to recent H α results, described below.

Next, consider the effects of the velocity gradient. Fig. 10 shows that increasing β from 1 to 2.5 (which corresponds to reducing the velocity gradient at $x = 1$ by a factor of 7.5 for $w_0 = 0.01$), decreases the inferred $\dot{M}(\text{IR})$ by a factor of 2.7. Thus, a large reduction in the velocity gradient can also strongly influence the mass-loss inferred from the IR flux.

It is interesting to compare our results with the recent H α mass-loss rates determined by Ramírez-Agudelo et al. (2017). For stars more luminous than $\log L/L_{\odot} \gtrsim 5.6$ (which corresponds roughly to $\dot{M}(\text{Vink}) \gtrsim 10^{-6} M_{\odot} \text{ yr}^{-1}$) both approaches require similar volume filling factors to bring the observational mass-loss rates into accord with the theoretical ones. However, at lower luminosity, the IR mass-loss rates are much larger than those determined from H α . This can arise if the velocity gradient is small, so that the opacity at continuum wavelengths is much less than in a line like H α . In this case, the IR emission probes more deeply into the wind and, as we saw above, a slow acceleration can greatly enhance the IR emission. Therefore, to avoid extremely large values of f_v , it seems that some combination of strong density clumping and a small acceleration at the base of the wind are required to produce the observed IR excesses. Given that the IR emission in stars expected to have low mass-loss rates originates in the poorly understood transition region between the photosphere and wind, our results should not be too surprising. Instead, we should view the IR as providing important constraints on the structure of the photosphere – wind interface.

A few other aspects of Fig. 7 are also of interest. First, the large intrinsic scatter in $\dot{M}(\text{IR})$ for stars with smaller $\dot{M}(\text{Vink})$ suggests that either the IR excesses are affected by physical parameters beyond those used to determine $\dot{M}(\text{Vink})$ (e.g. rotation, magnetic fields, interacting binary winds or incipient discs), or that the excesses in these stars are variable. Secondly, points from both the SMC and LMC overlap, implying that the physical origin of the process causing the additional excesses is independent of metallicity, and consistent with the Vink et al. (2001) treatment of different metallicities.

Our results could also have bearing on the ‘weak wind problem’ (Martins et al. 2005). If the excesses for low luminosity stars are due to extremely compact structures and small velocity gradients near the stellar surfaces, then many of the diagnostics used to interpret weak winds could be strongly affected.

ACKNOWLEDGEMENTS

DM acknowledges support from ADP Grant No.NNX14AB30G to SSI. This publication makes use of data products from the 2MASS, which is a joint project of the University of Massachusetts and the Infrared Processing and Analysis Center/California Institute of Technology, funded by the National Aeronautics and Space Administration and the National Science Foundation.

REFERENCES

Abbott D. C., Biegging J. H., Churchwell E., 1981, ApJ, 250, 645
 Abbott D. C., Telesco C. M., Wolff S. C., 1984, ApJ, 279, 225
 Blair W. P., Oliveira C., LaMassa S., Gutman S., Danforth C. W., Fullerton A. W., Sankrit R., Gruendl R., 2009, PASP, 121, 634
 Bonanos A. Z. et al., 2009, AJ, 138, 1003
 Bonanos A. Z. et al., 2010, AJ, 140, 416

Cassinelli J. P., Miller N. A., Waldron W. L., MacFarlane J. J., Cohen D. H., 2001, ApJ, 554L, 55
 Castor J. I., Simon T., 1983, ApJ, 265, 304
 Castor J. I., Abbott D. C., Klein R. I., 1975, ApJ, 195, 157 (CAK)
 Cranmer S. R., Owocki S. P., 1996, ApJ, 462, 469
 Crowther P. A. et al., 2016, MNRAS, 458, 624
 Ebbets D., 1982, ApJS, 48, 399
 Evans C. J., Lennon D. J., Trundle C., Heap S. R., Lindler D. J., 2004, ApJ, 607, 451
 Fitzpatrick E. L., Massa D., 2005, AJ, 129, 1642
 Fitzpatrick E. L., Massa D., 2009, ApJ, 699, 1209
 Fullerton A. W., Massa D. L., Prinja R. K., 2006, ApJ, 637, 1025
 Gordon K. D., Clayton G. C., 1998, ApJ, 500, 816
 Gordon K. D. et al., 2011, AJ, 142, 102
 Kaper L., Henrichs H. F., Nichols J. S., Telting J. H., 1999, A&A, 344, 231
 Kato D. et al., 2007, PASJ, 59, 615
 Lamers H. J. G. L. M., Waters L. B. F. M., 1984a, A&A, 136, 37 (LWa)
 Lamers H. J. G. L. M., Waters L. B. F. M., 1984b, A&AS, 57, 327 (LWb)
 Lanz T., Hubeny I., 2003, ApJS, 146, 41
 Lobel A., Blomme R., 2008, ApJ, 678, 408
 Martins F., Palacios A., 2017, A&A, 598A, 56
 Martins F., Plez B., 2006, A&A, 457, 637
 Martins F., Schaerer D., Hillier D. J., Meynadier F., Heydari-Malayeri M., Walborn N. R., 2005, A&A, 441, 735
 Massa D., Prinja R. K., 2015, ApJ, 809, 12
 Massa D., Fullerton A. W., Sonneborn G., Hutchings J. B., 2003, ApJ, 586, 996
 Massa D., Oskinova L., Fullerton A. W., Prinja R. K., Bohlender D. A., Morrison N. D., Blake M., Pych W., 2014, MNRAS, 441, 2173
 Massey P., Lang C. C., DeGioia-Eastwood K., Garmany C. D., 1995, ApJ, 438, 188
 Massey P., Bresolin F., Kudritzki R. P., Puls J., Pauldrach A. W. A., 2004, ApJ, 608, 1001
 Massey P., Puls J., Pauldrach A. W. A., Bresolin F., Kudritzki R. P., Simon T., 2005, ApJ, 627, 477
 Massey P., Zangari A. M., Morrell N. I., Puls J., DeGioia-Eastwood K., Bresolin F., Kudritzki R.-P., 2009, ApJ, 692, 618
 Meixner M. et al., 2006, AJ, 132, 2268
 Mokiem M. R. et al., 2007, A&A, 473, 603
 Owocki S. P., Castor J. I., Rybicki G. B., 1988, ApJ, 335, 914
 Panagia N., Felli M., 1975, A&A, 39, 1
 Penny L. R., Gies D. R., 2009, ApJ, 700, 844
 Petrov B., Vink J. S., Gräfener G., 2014, A&A, 565, A62
 Prinja R. K., Massa D., 2010, A&A, 521, L55
 Prinja R. K., Massa D., Fullerton A. W., 2002, A&A, 388, 587
 Prinja R. K., Massa D. L., Urbaneja M. A., Kudritzki R.-P., 2012, MNRAS, 422, 3142
 Puls J. et al., 1996, A&A, 305, 171
 Puls J., Markova N., Scuderi S., Stanghellini C., Taranova O. G., Burnley A. W., Howarth I. D., 2006, A&A, 454, 625
 Ramírez-Agudelo O. H. et al., 2017, A&A, 600A, 81
 Rauw G. et al., 2015, A&A, 580A, 59
 Rosendhal J. D., 1973a, ApJ, 182, 523
 Rosendhal J. D., 1973b, ApJ, 186, 909
 Schlafly E. F. et al., 2016, ApJ, 821, 78
 Schlafly E. F., Peek J. E. G., Finkbeiner D. P., Green G. M., 2017, ApJ, 838, 36
 Skrutskie M. F. et al., 2006, AJ, 131, 1163
 Sundqvist J. O., Puls J., Feldmeier A., 2010, A&A, 510, A11
 Underhill A. B., 1961 PDAO, 11, 353
 Vink J. S., de Koter A., Lamers H. J. G. L. M., 2001, A&A, 369, 574
 Weidner C., Vink J. S., 2010, A&A, 524, A98
 Weingartner J. C., Draine B. T., 2001, ApJ, 548, 296
 Wright A. E., Barlow M. J., 1975, MNRAS, 170, 41
 Šurlan B., Hamann W.-R., Kubàt J., Oskinova L. M., Feldmeier A., 2012, A&A, 541A, 37

SUPPORTING INFORMATION

Supplementary data are available at [MNRAS](#) online.

Table 1. SMC stellar properties.

Table 2. LMC stellar properties.

Table 3. SMC wind properties.

Table 4. LMC wind properties.

Please note: Oxford University Press is not responsible for the content or functionality of any supporting materials supplied by the authors. Any queries (other than missing material) should be directed to the corresponding author for the article.

This paper has been typeset from a $\text{T}_{\text{E}}\text{X}/\text{L}^{\text{A}}\text{T}_{\text{E}}\text{X}$ file prepared by the author.